

Transformer-based Hand Gesture Recognition via High-Density EMG Signals: From Instantaneous Recognition to Fusion of Motor Unit Spike Trains

Mansoorh Montazerin¹, Elahe Rahimian², Farnoosh Naderkhani², S. Farokh Atashzar^{3,4}, Svetlana Yanushkevich⁵, and Arash Mohammadi^{1,2,*}

¹Department of Electrical and Computer Engineering, Concordia University, Montreal, QC, Canada

²Concordia Institute for Information Systems Engineering, Concordia University, Montreal, QC, Canada

³New York University (NYU), Departments of Electrical & Computer Engineering and Mechanical & Aerospace Engineering, New York, 10003, NY, USA

⁴New York University (NYU), NYU WIRELESS, and NYU Center for Urban Science and Progress (CUSP), New York, 10003, NY, USA

⁵Department of Electrical and Software Engineering, Biometric Technologies Laboratory, Schulich School of Engineering, University of Calgary, Calgary, AB, Canada

*arash.mohammadi@concordia.ca

ABSTRACT

Designing efficient and labor-saving prosthetic hands requires powerful hand gesture recognition algorithms that can achieve high accuracy with limited complexity and latency. In this context, the paper proposes a compact deep learning framework referred to as the CT-HGR, which employs a vision transformer network to conduct hand gesture recognition using high-density sEMG (HD-sEMG) signals. Taking advantage of the attention mechanism, which is incorporated into the transformer architectures, our proposed CT-HGR framework overcomes major constraints associated with most of the existing deep learning models such as model complexity; requiring feature engineering; inability to consider both temporal and spatial information of HD-sEMG signals, and; requiring a large number of training samples. The attention mechanism in the proposed model identifies similarities among different data segments with a greater capacity for parallel computations and addresses the memory limitation problems while dealing with inputs of large sequence lengths. CT-HGR can be trained from scratch without any need for transfer learning and can simultaneously extract both temporal and spatial features of HD-sEMG data. Additionally, the CT-HGR framework can perform instantaneous recognition using sEMG image spatially composed from HD-sEMG signals. A variant of the CT-HGR is also designed to incorporate microscopic neural drive information in the form of Motor Unit Spike Trains (MUSTs) extracted from HD-sEMG signals using Blind Source Separation (BSS). This variant is combined with its baseline version via a hybrid architecture to evaluate potentials of fusing macroscopic and microscopic neural drive information. The utilized HD-sEMG dataset involves 128 electrodes that collect the signals related to 65 isometric hand gestures of 20 subjects. The proposed CT-HGR framework is applied to 31.25, 62.5, 125, 250 ms window sizes of the above-mentioned dataset utilizing 32, 64, 128 electrode channels. The average accuracy over all the participants using 32 electrodes and a window size of 31.25 ms is 86.23%, which gradually increases till reaching 91.98% for 128 electrodes and a window size of 250 ms. The CT-HGR achieves accuracy of 89.13% for instantaneous recognition based on a single frame of HD-sEMG image. The proposed model is statistically compared with a 3D Convolutional Neural Network (CNN) and a Support Vector Machine (SVM) model. The results corroborate effectiveness of the proposed framework compared to its counterparts.

1 Introduction

Hand gesture recognition using surface Electromyogram (sEMG) signals has been a topic of growing interest for development of assistive systems to help individuals with amputated limbs. Generally speaking, myoelectric prosthetic devices work by classifying existing patterns of the collected sEMG signals and synthesizing the intended gestures¹. While conventional myoelectric control systems, e.g., on/off control or direct-proportional, have potential advantages, challenges such as limited Degree of Freedom (DoF) due to crosstalk have resulted in the emergence of data-driven solutions. More specifically, to improve efficiency, intuitiveness, and the control performance of hand prosthetic systems, several Artificial Intelligence (AI) algorithms ranging from conventional Machine Learning (ML) models to highly complicated Deep Neural Network (DNN) architectures have been designed for sEMG-based hand gesture recognition in myoelectric prosthetic devices²⁻⁵. The ML-based models encompass traditional approaches such as Support Vector Machines (SVMs), Linear Discriminant Analysis (LDA),

and k -Nearest Neighbors (kNNs)⁶⁻⁹, and DNN-based models consist of frameworks such as Convolutional Neural Networks (CNNs), Recurrent Neural Networks (RNNs), and Transformer-based architectures¹⁰⁻¹⁵.

sEMG signals represent the electrical activities of the muscles and are recorded by a set of non-invasive electrodes that are placed on the muscle tissue^{16,17}. Broadly speaking, there are two types of sEMG acquisition systems, called sparse and high-density^{18,19}. Both of these groups are obtained by placing electrodes on the surface of the muscle and recording the electrical activity of the muscle's motor unit action potentials in response to the neural signals. Unlike sparse sEMG acquisition that involves a limited number of electrodes to record muscle activities, High-density sEMG (HD-sEMG) signals are obtained through a two-dimensional (2D) grid of electrodes, which cover an area of the muscle tissue and a large number of associated motor units^{20,21}. It is, therefore, more difficult to design an ML/DL-based algorithm for hand gesture recognition from HD-sEMG signals as they require more computational power for the signal processing and training stages. However, HD-sEMG signals are considered more potent than their sparse counterparts because of their ability to include both temporal and spatial information of muscle activities, which provides a high-resolution 3-dimensional signal (two dimensions in space and one in time)²². The HD-sEMG signal acquisition can evaluate functionality of the underlying neuromuscular system more precisely in terms of spatial resolution. Accordingly, developing an efficient DNN-based framework that can effectively learn from a comprehensive HD-sEMG dataset is of great importance in neuro-rehabilitation research and clinical trials²³, which is the focus of this manuscript.

Conventional ML models, such as SVMs and LDAs, utilized for sEMG-based hand gesture recognition, typically work well when dealing with small datasets. These methods, however, depend on manual extraction of handcrafted (engineered) features, which limits their generalizability as human knowledge is needed to find the best set of features²⁴. Increasing the number of utilized electrodes and the number of gestures entails extracting more features, therefore, the feature extraction process becomes significantly complex and time-consuming. This is because more trials and efforts are required to boost the discriminative power of the model. Dependence on engineered features is partially/fully relaxed by utilization of DNN-based models. Among the most frequently used DNN architectures for the task of hand gesture recognition is the CNN-based frameworks. For example, Reference¹² converts sEMG signals to 3D images and uses transfer learning to feed them to a popular CNN trained on a database of natural images. CNNs, however, are designed to concentrate on learning spatial features of the input signals and fail to extract temporal features of the sEMG data. To overcome this issue, researchers turned their attention to hybrid CNN-RNN frameworks that were designed to take both spatial and temporal information of the time-series sEMG datasets into account^{25,26}. For instance, Hu *et al.*²⁵ have applied attention mechanism on top of a hybrid CNN-LSTM model to perform hand gesture recognition based on sEMG signals with relatively large window sizes (i.e. 150 ms and 200 ms). They achieved classification accuracy of up to 87% using the largest window size. In²⁶, a dimensionality reduction method is proposed and assumed to enhance the classification accuracy when used with a hybrid CNN-LSTM architecture. In this framework²⁶, the classification accuracy is 88.9% on the same dataset as that of²⁵ for the 250 ms window size. Nonetheless, as well as not allowing entire input parallelization, hybrid CNN-RNN frameworks are usually computationally demanding and reveal important limitations with respect to the memory usage and large training times. In this paper, we aim to eliminate the complexity of simultaneously exploiting CNNs and RNNs by introducing a Vision Transformer-based (ViT)²⁷ architecture to be applied on HD-sEMG signals and to efficiently deal with the above-mentioned constraints.

In this study, a comprehensive evaluation of the proposed ViT-based framework for hand gesture classification on HD-sEMG dataset is carried out for the first time to the best of our knowledge. The ViT architecture takes advantage of the attention²⁸ mechanism, which works by finding dependencies and similarities among different data portions. The attention mechanism in the ViT is integrated in a typical transformer model, making it a robust framework for hand gesture recognition without being combined with other DL algorithms. One of the differences between the ViT and a typical transformer is that the ViT is generally designed to be applied on 3D images rather than 2D time-series signals. Considering the fact that HD-sEMG signals comprise of two dimensions in space and one in time (3 dimensions in total), they can be an appropriate input to a ViT. As mentioned in²⁹, instantaneous training with HD-sEMG signals refers to training the network with a 2D image depicting motor unit action potential activities under a grid of electrodes at a single time point. In this paper, we also show that there are reproducible patterns among instantaneous samples of a specific gesture which could also be a physiological representation of muscle activities in each time point. We demonstrate that the proposed framework can perform instantaneous hand gesture classification using sEMG image spatially composed from HD-sEM. In other words, it can achieve acceptable accuracy when receiving, as an input, a single frame of the HD-sEMG image. The main contributions of the paper are briefly outlined below:

- To the best of our knowledge, the proposed CT-HGR is the first ViT-based architecture that is leveraged to classify hand gestures from HD-sEMG signals. It can efficiently classify a large number of hand gestures relying only on the attention mechanism. Furthermore, the CT-HGR can be trained from scratch without the need for transfer learning or data augmentation.
- Achieving high accuracy over small windows sizes, e.g., 32 ms, which has been rarely worked on in the previous literature. This can be a remarkable milestone for hand prosthetic systems to operate with low latency.

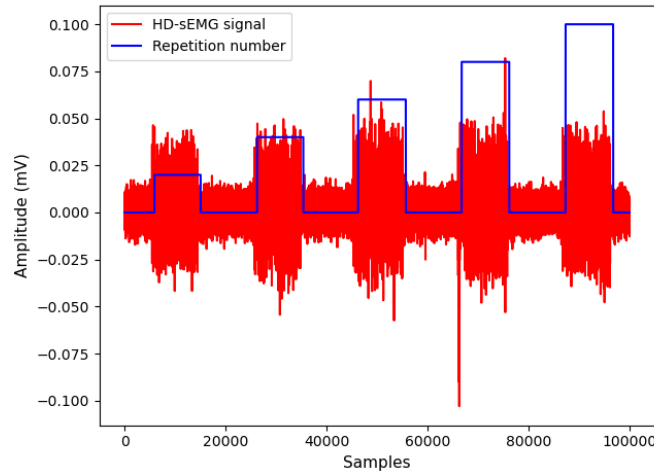


Figure 1. Illustration of the raw HD-sEMG dataset. The red plot is the sEMG signal and the blue plot shows the exact location of movements and their repetition number.

- Achieving near baseline accuracy using instantaneous HD-sEMG data samples, which is significant as it paves the way for real-time learning from HD-sEMG signals.
- Introducing, for the first time to the best of our knowledge, the idea of integrating macroscopic and microscopic neural drive information through a hybrid DNN framework. The proposed variant of the CT-HGR framework, is a hybrid model that simultaneously extracts a set of temporal and spatial features through its two independent ViT-based parallel architectures (the so called Macro and Micro paths). The Macro Path is the baseline CT-HGR model, while the Micro path is fed with the p-to-p values of the extracted Motor Unit Action Potentials (MUAPs) of each source.

The rest of the paper is structured as follows: The utilized HD-sEMG dataset is introduced in Sub-Section 2.1. An explanation of the pre-processing procedures on the raw dataset is given in Sub-section 2.2 and our proposed framework is presented in Sub-section 2.3. Our experiments and evaluations of implementing the proposed framework are discussed in Section 3 and finally, Section 4 concludes the paper.

2 Materials and Methods

2.1 The HD-sEMG Dataset

The dataset³⁰ used in this study is a recently released HD-sEMG dataset that contains two 64-electrode square grids (8×8) with an inter-electrode distance of 10 mm, which were placed on extensor and flexor muscles of 20 participants. One of the subjects is not included in the study from the beginning due to its incomplete information. The participants performed 65 hand gestures that are combinations of 16 basic single degree of freedom movements. One of the gestures is carried out twice, therefore, there are 66 movements in total. The subjects performed each gesture 5 times with 5 seconds rest in between. Fig. 1 illustrates how the raw dataset is organized. The red plot shows the HD-sEMG signal acquired for all the 5 repetitions of one specific hand movement. The blue line shows the repetition number of the gesture and the rest intervals. The signals were recorded through a Quattrocento (OT Bioelettronica, Torino, Italy) bioelectrical amplifier system with 2,048 Hz sampling frequency. Signals of the successive channels were subtracted from each other to lower the amount of common-mode noise. The rationale behind selection of this publicly available dataset is that it comprises of a large number of gestures and electrodes, which allows development of a generalizable framework by investigating different settings of the input data. Additionally, this dataset provides straightforward instructions on how to deploy the dataset for different evaluation purposes. However, since the paper³⁰ on this dataset did not refer to the train and test sets as a basis for comparison, we performed a 5-fold cross-validation as there are 5 sessions in the dataset. In this way, one (out of 5) repetition is considered as the test set and the remaining are assigned to the train set. Each time, the test set is changed until all the repetitions have been tested. Finally, the accuracy of each fold together with the average accuracy across all the folds are reported.

2.2 Data Pre-processing

The raw HD-sEMG dataset is pre-processed in three distinct steps before being fed to the proposed CT-HGR framework. More specifically, the pre-processing steps in this study consist of low-pass filtering, normalization, and windowing. During hand

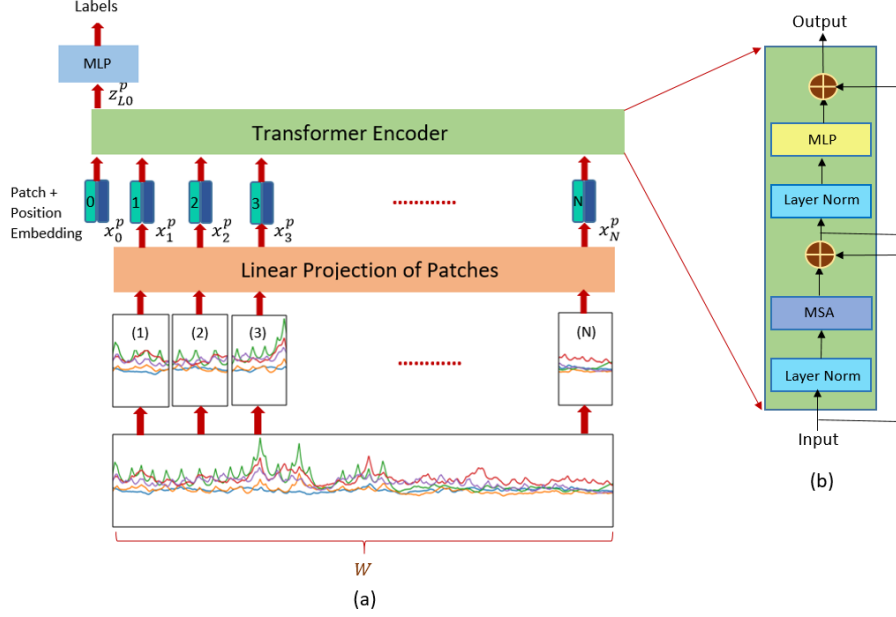


Figure 2. Overview of the CT-HGR network. (a) The windowed HD-sEMG signal is fed to the CT-HGR and split into smaller patches. The patches go through a linear projection layer which converts them from 3D to 2D data samples. A class token is added to the patches and the $N + 1$ patches are input to a transformer encoder. Ultimately, the first output of the transformer corresponding to the class token is chosen for the multi-class classification part. (b) This is the transformer encoder which is the fundamental part of the ViT, responsible for processing the input patches.

movement recording, sEMG signals were filtered with a 10-Hz high-pass. However, following several experiments and based on the previous literature^{29, 31–33}, we deduced that the wide variations in the sEMG signals prevent the model from learning key features properly. Thus, a low-pass first-order butterworth filter at 1 Hz is applied separately to each of the 128 channels of the data to derive the positive envelope of the main signal. In the next pre-processing phase, the filtered signals are normalized by the μ -law normalization algorithm, which reduces significant changes in the dynamic range of the signals acquired from different electrodes. The μ -law normalization is performed based on the following formulation

$$F(x_t) = \text{sign}(x_t) \frac{\ln(1 + \mu|x_t|)}{\ln(1 + \mu)}, \quad (1)$$

where x_t is the time-series sEMG signal for each electrode channel, and μ is the extent to which the signals are scaled down and is determined empirically. According to^{2, 34}, μ -law normalization helps the network to learn gestures more effectively. The final pre-processing stage is to segment the sEMG signals. After removing the rest intervals from the dataset, the signals are segmented with a specific window size creating the main 3D input of the CT-HGR with shape $W \times N_{ch} \times N_{cv}$, where W is the window size and N_{ch} and N_{cv} are the number of horizontal and vertical channels respectively. This completes our discussion on the pre-processing stage. In what follows, the proposed CT-HGR framework is presented, which takes the pre-processed data samples as its input and returns the predicted gesture class.

2.3 The Proposed CT-HGR

In this section, description of our proposed CT-HGR framework, its main building blocks, and its adoption for the task of hand gesture recognition are presented. The CT-HGR is developed based on the ViT network in which the attention mechanism is utilized to understand the temporal and spatial connections among multiple data segments of the input. As stated previously, several studies have employed the attention mechanism together with hybrid CNN-RNN models to force the network to learn both spatial and temporal information of the signals^{3, 25}. However, in this paper, we demonstrate that attention mechanism can work independently of any other network and achieve high accuracy when trained from scratch with no data augmentation. We also show that the proposed framework can be trained even on pretty small window sizes and more importantly on instantaneous data samples.

An overall illustration of the CT-HGR is indicated in Fig. 2. After completion of the pre-processing steps discussed in the previous section, we have 3D signals of shape $W \times N_{ch} \times N_{cv}$, where W is the window size and N_{ch} and N_{cv} are the number of horizontal and vertical channels respectively. The utilized window sizes in our experiments are mainly of 64, 128, 256, and 512

data points (31.25, 62.5, 125, and 250 ms respectively). We choose the window sizes to be the powers of 2 because it provides us with more flexibility in patching the data segments after being fed to the ViT³⁵. Furthermore, we have assessed the effect of changing the number of electrode channels by using 32, 64 and 128 out of the whole 128 channels. Therefore, we set N_{ch} to 4, 8, and 16 each time while N_{cv} remains constant at 8. In what follows, the major blocks of the proposed CT-HGR network, namely “Patch Embedding”, “Position Embedding”, “Transformer Encoder”, and the “Multilayer Perceptron” blocks.

2.3.1 Patch Embedding

In this block, the 3D signals are divided into N small patches either horizontally, vertically or both. Therefore, we have N patches of size $H \times V \times N_{cv}$ that are then linearly flattened to 2D signals of size $N \times HVN_{cv}$ where, N is equal to WN_{ch}/HV and is the effective sequence length of the transformer’s input. Consequently, there are N patch vectors \mathbf{x}_i^p , for $(1 \leq i \leq N)$. Using a trainable linear projection layer, the \mathbf{x}_i^p vectors are embedded with the model’s dimension d . The linear projection is shown with matrix \mathbf{E} , which is multiplied to each of the \mathbf{x}_i^p and yields N vectors of dimension d . Moreover, a class token named \mathbf{x}_0^p similar to what was previously used in the Bert framework³⁶ is prepended to the aforementioned vectors to gather all the useful information learned during the training stage and is used in the final step when different hand gestures are classified. The final sequence length of the transformer after adding the class token is $N + 1$.

2.3.2 Position Embedding

Unlike RNNs that process their inputs sequentially, transformers apply the attention mechanism to all of the data segments in parallel, which deprives them of the capacity to intrinsically learn about the relative position of each patch of a single input. Because sEMG signals are time-series sequences of data points in which the location of each point matters for hand gesture classification tasks, we need to train the network to assign a specific position to each sample. Generally speaking, positional embedding is an additional piece of information that is injected into the network, helping it to identify how data points are ordered. There are different types of positional embeddings offered such as relative, 1D, 2D, and sinusoidal positional embeddings that may be learnable or non-learnable. In this context, we use a learnable 1D positional embedding vector that is added to each of the embedded \mathbf{x}_i^p vectors to maintain and learn the position of each patch during the training phase. The final output z_0 of the “Patch + Position Embedding” blocks is given by

$$z_0 = [\mathbf{x}_0^p; \mathbf{x}_1^p \mathbf{E}; \mathbf{x}_2^p \mathbf{E}; \dots; \mathbf{x}_N^p \mathbf{E}] + \mathbf{E}^{pos}, \quad (2)$$

where \mathbf{E}^{pos} is an $(N + 1) \times d$ matrix, holding the relative position of each patch in a d -dimensional vector.

2.3.3 Transformer Encoder

A typical transformer model consists of two major parts called encoder and decoder. In this paper, we aim to utilize only the former part. The transformer encoder is where the attention mechanism tries to find the similarities among the $N + 1$ patches that arrive at its input. As can be seen in Fig. 2(b), there are L identical layers of transformer encoder in the CT-HGR network and each has three separate blocks, named as “Layer Norm”, “Multi-head Self Attention (MSA)” and “MLP”. The z_0 sequence of patches that is explained above is first fed to a normalization layer to improve the generalization performance of the model and accelerate the training process³⁷. The “Layer Norm block” is then followed by the MSA module, which incorporates h parallel blocks (heads) of the scaled dot-product attention (also known as self attention). In the context of self attention, three different vectors *Keys*(K), *Queries*(Q) and *Values*(V) of dimension d are employed for each input patch. For computing the self attention metric, the dot product of *Queries* and all the *Keys* are calculated and scaled by $1/\sqrt{d}$ in order to prevent the dot products from generating very large numbers. This matrix is then, converted into a probability matrix through a *softmax* function and is multiplied to the *Values* to produce the attention metric as follows

$$Attention = softmax\left(\frac{QK^T}{\sqrt{d}}\right)V. \quad (3)$$

In the MSA block, instead of dealing with d -dimensional *Queries*, *Keys* and *Values*, we split them into h parallel heads and measure the self attention metric on these heads independently. Finally, after finding the corresponding results for each head, we concatenate them to obtain the d -dimensional vectors of patches. As indicated in Fig. 2(b), residual paths from the encoder’s input to the output of the MSA block are employed to avoid the gradient vanishing problem. The formulations for the above explanations are as follows

$$z'_l = MSA(LayerNorm(z_{l-1})) + z_{l-1}, \quad (4)$$

$$z_l = MLP(LayerNorm(z'_l)) + z'_l, \quad (5)$$

where z_l is the l^{th} transformer layer’s output and $l = 1, \dots, L$. The final output of the transformer encoder is given by

$$z_L = [z_{L0}^p; z_{L1}^p; \dots; z_{LN}^p], \quad (6)$$

Table 1. Comparison of classification accuracy and STD for each fold and their average for different window sizes and number of channels (CT-HGR-V1). The accuracy and STD for each fold is averaged over 19 subjects.

# Channels	Window size	Fold1(%)	Fold2	Fold3	Fold4	Fold5	Average
32	64	76.85 (± 3.83)	89.30 (± 2.61)	89.91 (± 2.54)	89.62 (± 2.67)	85.49 (± 3.07)	86.23 (± 2.94)
	128	77.21 (± 3.56)	89.48 (± 2.60)	90.05 (± 2.63)	90.00 (± 2.61)	85.83 (± 2.96)	86.51 (± 2.87)
	256	77.63 (± 3.50)	90.51 (± 2.52)	90.79 (± 2.45)	90.99 (± 2.42)	86.66 (± 2.97)	87.32 (± 2.77)
64	64	79.64 (± 3.38)	91.92 (± 2.41)	92.55 (± 2.18)	92.37 (± 2.32)	88.16 (± 2.77)	88.93 (± 2.61)
	128	80.26 (± 3.44)	92.32 (± 2.27)	92.94 (± 2.20)	92.48 (± 2.22)	88.46 (± 2.77)	89.29 (± 2.58)
	256	81.43 (± 3.31)	92.89 (± 2.15)	93.42 (± 2.13)	93.05 (± 2.18)	89.29 (± 2.69)	90.02 (± 2.49)
128	64	82.14 (± 3.26)	93.30 (± 2.14)	93.75 (± 2.08)	93.39 (± 2.11)	90.07 (± 2.55)	90.53 (± 2.43)
	128	82.80 (± 3.22)	93.47 (± 2.13)	93.98 (± 2.03)	93.82 (± 2.10)	90.30 (± 2.48)	90.87 (± 2.39)
	256	83.20 (± 3.21)	94.19 (± 2.00)	94.25 (± 1.97)	94.42 (± 1.91)	90.70 (± 2.46)	91.35 (± 2.31)
	512	83.87 (± 3.21)	94.62 (± 1.88)	95.26 (± 1.80)	94.89 (± 1.85)	91.26 (± 2.37)	91.98 (± 2.22)

Table 2. Comparison of classification accuracy and STD for each fold and their average for different window sizes and 128 electrode channels (CT-HGR-V2). The accuracy and STD for each fold is averaged over 19 subjects.

# Channels	Window size	Fold1(%)	Fold2	Fold3	Fold4	Fold5	Average
128	64	83.82 (± 3.22)	94.03 (± 2.02)	94.58 (± 1.9)	94.29 (± 2.05)	90.84 (± 2.58)	91.51 (± 2.35)
	128	83.98 (± 3.17)	94.09 (± 2.00)	94.82 (± 1.86)	94.65 (± 1.94)	90.89 (± 2.45)	91.69 (± 2.28)
	256	84.74 (± 3.13)	94.60 (± 1.92)	95.19 (± 1.80)	95.06 (± 1.86)	91.59 (± 2.44)	92.24 (± 2.23)
	512	85.27 (± 3.12)	95.55 (± 1.70)	95.81 (± 1.65)	95.60 (± 1.73)	92.16 (± 2.32)	92.88 (± 2.10)

where $z_{L_i}^p$ is the final layer’s output corresponding to the i^{th} patch and $i = 1, \dots, N$. As mentioned before, among all the above vector of patches, the $z_{L_0}^p$ vector matching the class token is chosen for gesture classification. Authors in²⁷ claim that the learned features in the sequence of patches will eventually be included in the class token, which has a decisive role in predicting the model’s output. Therefore, $z_{L_0}^p$ is passed to a linear layer which outputs the predicted gesture’s label as

$$y_{\text{predicted}} = \text{Linear}(z_{L_0}^p). \quad (7)$$

In the next section, we will describe the various experiments performed in this study and present the obtained results and their explanations in detail.

3 Results

We perform several experiments to evaluate performance of the proposed framework under different configurations. In the following, each of the conducted experiments and their corresponding results are presented separately. The implemented models are evaluated on all the 66 gestures of the HD-sEMG dataset performed by 19 healthy subjects. The implementations were developed in the PyTorch framework and the models are trained using an NVIDIA GeForce GTX 1080 Ti GPU.

3.1 Overall Performance Evaluation under Different Configurations

In this experiment, we employ 4 different window sizes together with 3 different combination of electrodes of the HD-sEMG dataset and report the achieved accuracy for each of the 5 test folds and the overall averaged accuracy. In the first model, referred to as the CT-HGR-V1, the simplest and smallest CT-HGR model that gives acceptable results is chosen. The length of windowed signals, in this model, is set to 64, 128, 256 and 512 (31.25, 62.5, 125, 250 ms respectively) with skip step of 32 except for the window size of 512 for which the skip step is set to 64. To measure effects of increasing the number of channels on the performance of the proposed architecture, we consider three different settings using all, half, and 1/4 of the 128 electrodes. In the half mode, electrodes of multiple of 2 and in the 1/4 mode, electrodes of multiple of 4 were chosen. As stated previously, the number of horizontal electrode channels in the CT-HGR’s input is 4, 8, and 16 while the number of vertical channels is 8. Regarding the hyperparameters of the model, the model’s (embedding) dimension is 64, and the patch size is set to (8, 4), (8, 8), and (8, 16) for 32, 64, and 128 number of channels, respectively. The CT-HGR-V1 model contains only 1 transformer layer and 8 heads. The MLP block’s hidden size is set to 64, the same as its input size. The CT-HGR-V1 model is trained with 20 epochs and batch size of 128 for each subject independently. The optimization method used is Adam with $\beta_1 = 0.9$ and $\beta_2 = 0.999$ parameters, learning rate of 0.0001 and weight decay of 0.001. Learning rate annealing is deployed

Table 3. The number of learnable parameters for different number of electrodes and window sizes.

# Channels	Window size	# Parameters (CT-HGR-V1)	# Parameters (CT-HGR-V2)	# Parameters (3D CNN)
32	64	46,530	-	-
	128	47,042	-	-
	256	48,066	-	-
64	64	62,914	-	294,914
	128	63,426	-	311,298
	256	64,450	-	319,490
128	64	95,682	273,346	-
	128	96,194	274,370	-
	256	97,218	276,418	-
	512	99,266	280,514	-

after the first 10 epochs for faster convergence. The cross-entropy loss function is considered as the objective function. Table 1 represents the acquired accuracy and standard deviation (STD) for each individual window size and number of channels. It is worth noting that the 512 window size is only tested with the whole electrode channels of the dataset to indicate the potential best performance of the network.

A second variant of the CT-HGR model, referred to as CT-HGR-V2, is also tested where the model’s dimension and the number of hidden layers in the MLP layer are twice those of CT-HGR-V1. We apply the CT-HGR-V2 model on the data samples derived from the whole 128 electrodes to compare it with the last 4 rows of Table 1. The results are shown in Table 2. Table 3 illustrates the number of learnable parameters for each window size and number of channels in both models.

Fig. 3 demonstrates the box plots for the accuracy of CT-HGR-V1 obtained for each individual fold and different window sizes from $W = 64$ to $W = 512$ (Fig. 3(a-d)). The box plots are drawn based on the interquartile range (IQR) of accuracy for 19 subjects when all the 128 electrodes are included in the experiment. The black horizontal line represents the median accuracy for each fold.

In Fig. 4, the Wilcoxon signed rank test is applied for CT-HGR-V1 and CT-HGR-V2 separately when the number of channels is fixed at 128. The box plots show the IQR for each window size that decreases minimally from CT-HGR-V1 to CT-HGR-V2. The Wilcoxon test’s p -value annotations in Fig. 4 are as follows:

- ns: $5.00e - 02 < p \leq 1.00e + 00$
- *: $1.00e - 02 < p \leq 5.00e - 02$
- **: $1.00e - 03 < p \leq 1.00e - 02$
- ***: $1.00e - 04 < p \leq 1.00e - 03$
- ****: $p \leq 1.00e - 04$

Although the average accuracy does not change significantly, the STD in CT-HGR-V2 with $W = 512$ declines significantly compared to CT-HGR-V1.

The gestures in the HD-sEMG dataset are ordered according to their DoF and similarity in performance. The simple 1 DoF gestures are labeled from 1 to 16, 2 DoF gestures are from 17 to 57 and the most complex ones are from 58 to 66. To be more specific, the confusion matrices for Model CT-HGR-V1 with $W = 512$ and 128 number of channels are obtained for all the subjects. The matrices are summed and normalized row-wise. The final confusion matrix is shown in Fig. 5. The diagonal values show the average accuracy acquired for each hand gesture among 19 subjects. The average accuracy for most of the gestures is above 94%. The density of the non-zero elements in Fig. 5 is utmost near the diagonal, which implies that the possibility of the network making mistakes in gesture classification is higher in gestures that have the same DoF and are performed similarly.

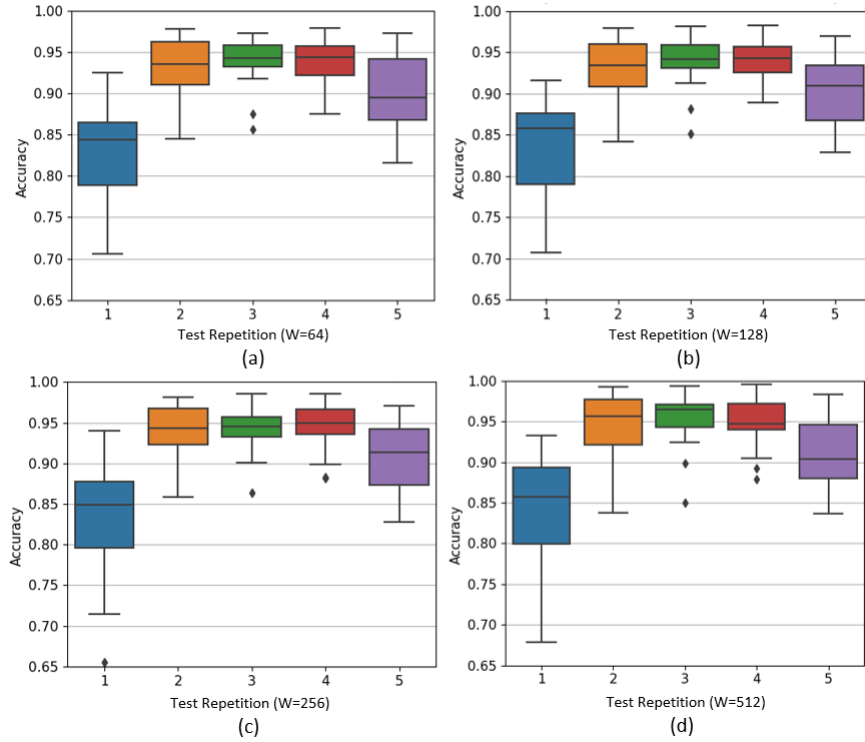


Figure 3. Comparison of the accuracy CT-HGR-V1 obtains for each fold and window sizes of (a) $W = 64$ (b) $W = 128$ (c) $W = 256$ and (d) $W = 512$. The number of utilized electrode channels in these plots is 128.

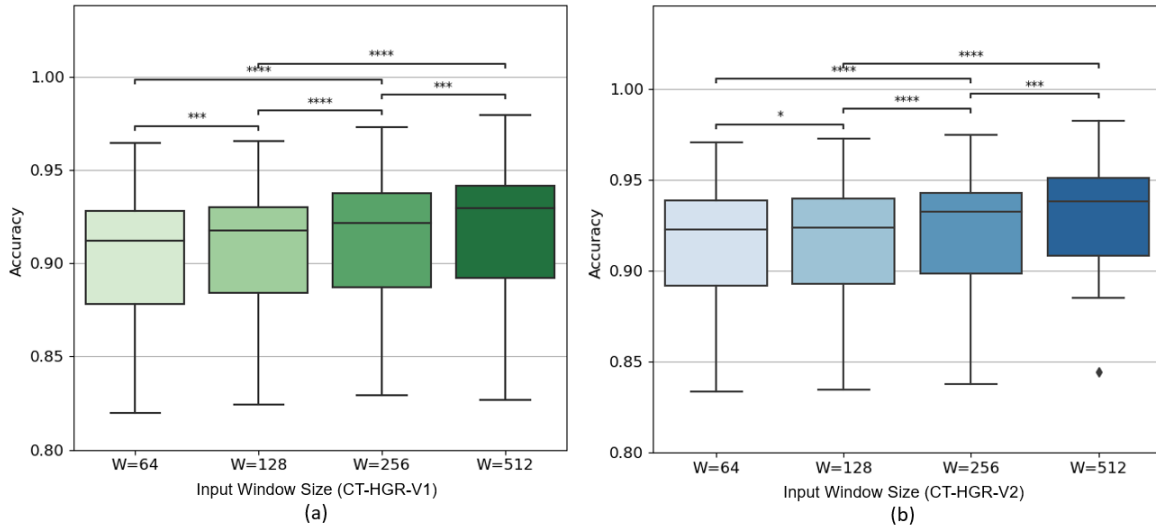


Figure 4. Box plots and IQR for different window sizes ($W = 64$, $W = 128$, $W = 256$, and $W = 512$) and 128 number of channels for CT-HGR- (a) V1 and (b) V2

3.2 Comparisons with a Conventional ML and a 3D Convolutional Model

In the first part of this sub-section, we provide comparison results with a traditional ML algorithm developed based on Support Vector Machines (SVM), which is commonly^{38–40} used for hand gesture recognition tasks. Following the works of References^{38–40}, we extract the four most popular feature sets that are used for ML classifiers from our dataset. Extracted features are as follows: Root Mean Square (RMS), Zero Crossings (ZC), Slope Sign Change (SSC), and Wavelength (WL), which are separately extracted for each electrode channels. In Table 4, the obtained results for the SVM model in which the

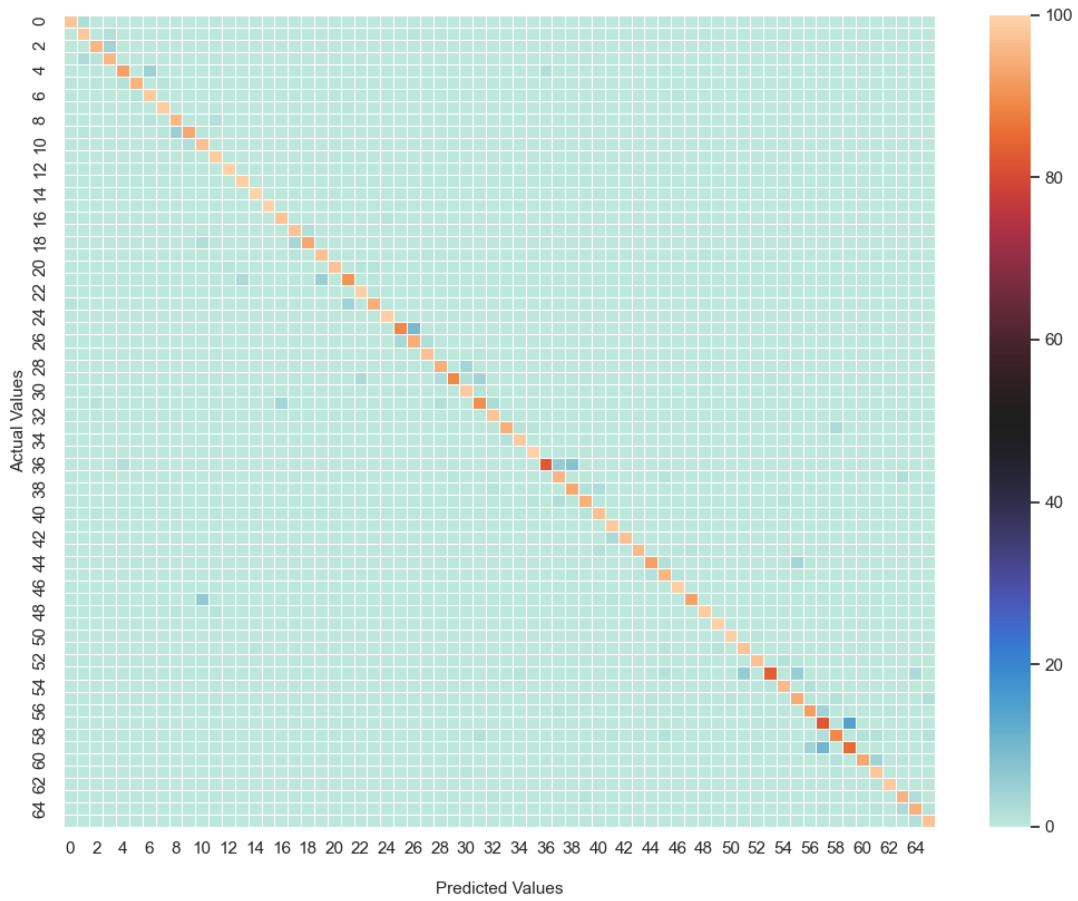


Figure 5. Average confusion matrix of Model CT-HGR-V1 with $W = 512$ and 128 number of electrodes over 19 subjects.

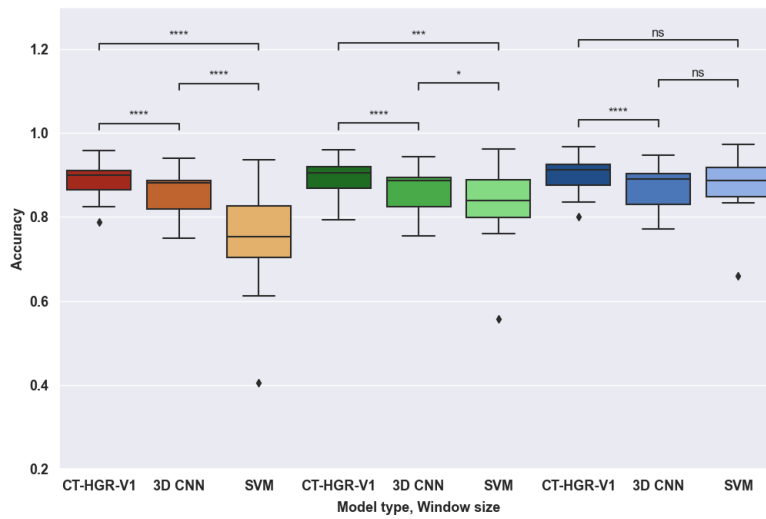


Figure 6. Box plots and IQR of CT-HGR-V1, 3D CNN and SVM for different window sizes ($W = 64$ $W = 128$ and $W = 256$) and 64 number of channels.

number of channels in the dataset is set to 64 are presented.

Table 4. Comparison of classification accuracy and STD of each fold and their average for different window sizes and 64 electrode channels using an SVM model. The accuracy and STD for each fold is averaged over 19 subjects.

# Channels	Window size	Fold1(%)	Fold2	Fold3	Fold4	Fold5	Average
64	64	63.62 (± 11.58)	77.62 (± 11.28)	78.99 (± 11.45)	78.12 (± 11.07)	73.42 (± 11.10)	74.35 (± 11.30)
	128	72.84 (± 10.47)	86.49 (± 8.32)	87.32 (± 8.11)	87.48 (± 8.12)	82.35 (± 8.66)	83.30 (± 8.74)
	256	77.74 (± 9.34)	90.95 (± 6.18)	91.56 (± 6.06)	91.01 (± 5.84)	87.41 (± 6.51)	87.73 (± 6.79)

Table 5. Comparison of classification accuracy and STD of each fold and their average for different window sizes and 64 electrode channels using a 3D CNN model. The accuracy and STD for each fold is averaged over 19 subjects.

# Channels	Window size	Fold1(%)	Fold2	Fold3	Fold4	Fold5	Average
64	64	75.90 (± 3.85)	89.19 (± 2.65)	90.36 (± 2.56)	89.81 (± 2.63)	85.51 (± 3.06)	86.15 (± 2.95)
	128	76.30 (± 3.73)	90.13 (± 2.56)	90.84 (± 2.42)	90.06 (± 2.57)	86.07 (± 2.98)	86.68 (± 2.85)
	256	77.63 (± 3.62)	90.56 (± 2.49)	90.95 (± 2.45)	90.95 (± 2.45)	87.14 (± 2.83)	87.45 (± 2.77)

Table 6. Accuracy and STD for the shuffled dataset of all the 5 repetitions and different window sizes (CT-HGR-V1).

# Channels	Window size	# Avg accuracy(%)
64	64	98.05 (± 1.19)
	128	98.43 (± 1.05)
	256	98.79 (± 0.96)

Table 7. Accuracy and STD of each fold and their average for instantaneous training.

# Channels	Window size	Fold1(%)	Fold2	Fold3	Fold4	Fold5	Average
64	1	80.02 (± 3.45)	92.33 (± 2.27)	92.47 (± 2.26)	92.16 (± 2.31)	88.69 (± 2.74)	89.13 (± 2.61)

In the second part, we implement a 3D CNN model that is originally utilized for video-based hand gesture recognition tasks⁴¹ and is found effective by authors in⁴² to be applied on HD-sEMG datasets as they resemble video data in having one dimension in time and two dimensions in space. Therefore, in spite of a typical 2D CNN model, a 3D CNN architecture is able to extract both the temporal and spatial features in HD-sEMG datasets. The 3D signals of shape $W \times N_{ch} \times N_{cv}$ go through the 3D CNN architecture that has two consecutive 3D CNN layers with 16 and 32 respective filters of size (5, 3, 3), each followed by a GELU activation function, a dropout and a max pooling layer. Then, two fully connected (FC) layers of size 256 and 128 are deployed before the output layers which consists of an MLP head similar to the one used in our CT-HGR models followed by a *softmax* function for classification. The other hyperparameters of the network are set similar to those of the CT-HGR model. The stride values in both 3D CNN layers are 1. Table 5 shows the acquired results for the 3D CNN model in which the number of channels in the dataset is set to 64.

Fig. 6 shows the box plots and the results of Wilcoxon signed rank statistical test that is conducted for comparing CT-HGR-V1 and SVM model’s accuracy on 19 subjects. In this experiment, only the models with the same window size are compared to assess the discrepancy between two different models with the same input data.

3.3 Performance Evaluation based on Shuffled Data

In the previous sub-sections, a 5-fold cross-validation was applied on the HD-sEMG dataset in which the test set (repetition) is entirely unseen and is not included in the train set (repetitions). However, another approach followed in the literature^{9,43} to split the two sets is to shuffle the whole dataset with 5 repetitions and assign 20% for the test set and 80% for the train set. In this scenario, the test set is unseen but data samples from the same repetitions may exist in both sets making the model more familiar with the test samples potentially achieving higher accuracy. The obtained average accuracy over 19 participants using 64, 128, 256 window sizes using the hyperparameters of CT-HGR-V1 are summarized in Table 6.

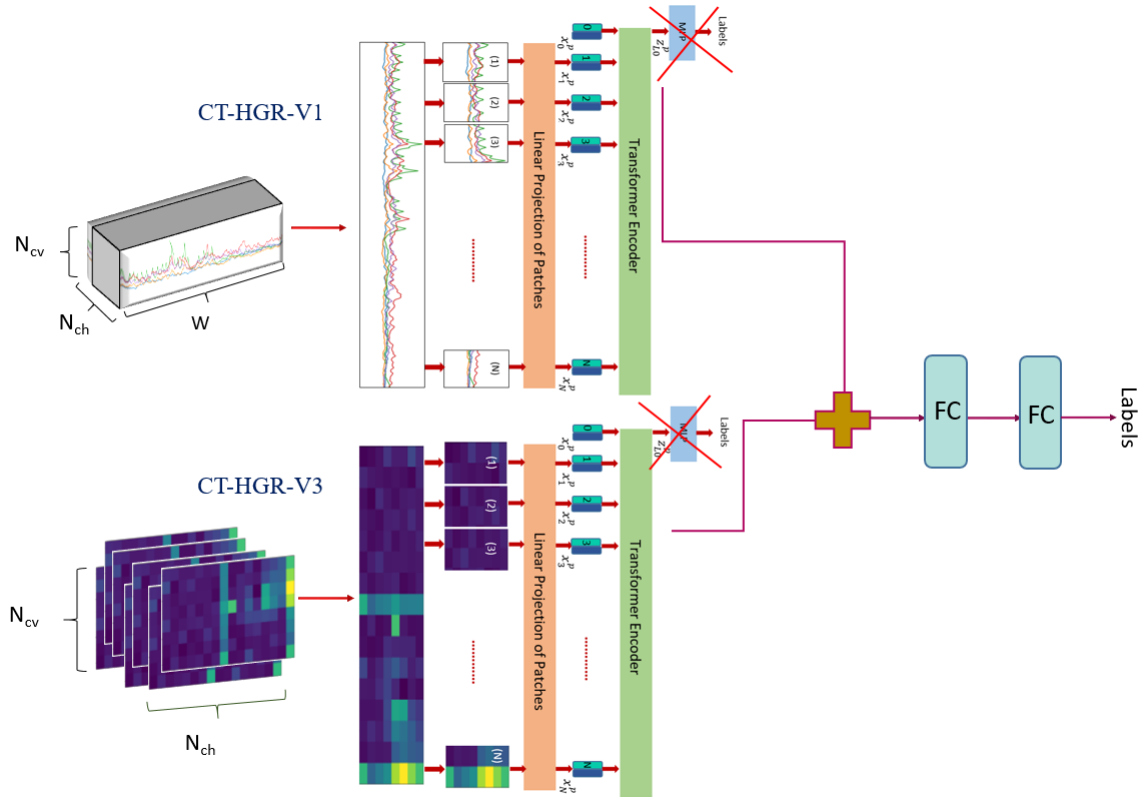


Figure 7. The fused CT-HGR framework. In the first stage, the ViT-based models in the Macro and Micro paths are trained based on 3D, HD-sEMG and 2D, p-to-p MUAP images, respectively. In the second stage, the Micro and Macro weights are frozen. The final Micro and Macro class tokens are concatenated and converted to a 1,024-dimensional feature vector, which is fed to a series of FC layers for gesture classification.

3.4 Instantaneous Performance Evaluation

In this sub-section, our objective is to assess the functionality of the proposed framework on instant HD-sEMG data points. In other words, we consider window size of only 1 sample as the input to our model, which requires no patching. We set the number of electrodes to 64. The hyperparameters used in this experiment are the same as those used for CT-HGR-V1. The accuracy results are presented in Table 7.

3.5 Evaluation of a Hybrid Model based on Raw HD-sEMG and Extracted MUAPs

In this sub-section, we present the results of fusing CT-HGR-V1 with a third variant of CT-HGR called CT-HGR-V3 that works based on the extracted MUAPs from raw HD-sEMG signals. Fig. 7 illustrates the overall hybrid architecture of the fused model. More specifically, CT-HGR-V3 uses HD-sEMG decomposition to extract microscopic neural drive information. sEMG decomposition refers to a set of Blind Source Separation (BSS) methods that extract discharge timings of motor neuron action potentials from raw HD-sEMG data. Single motor neuron action potentials are summed to form MUAPs that convert neural drive information to hand movements. Motor unit discharge timings, also known as Motor Unit Spike Trains (MUSTs), represent sparse estimations of the MU activation times with the same sampling frequency and time interval as the raw HD-sEMG signals. HD-sEMG signals can be modelled as a spatio-temporal convolution of MUSTs, which provide an exact physiological description of how each hand movement is encoded at neurospinal level. Thus, MUSTs are of trustworthy and discernible information on the generation details of different hand gestures, as such is adopted in CT-HGR-V3 for hand gesture recognition. For extracting MUSTs, among the existing BSS approaches⁴⁴ suggested for HD-sEMG decomposition, gradient Convolution Kernel Compensation (gCKC)^{45,46} and fast Independent Component Analysis (fastICA)⁴⁷ are of great prominence and frequently used in the literature. To achieve better accuracy, the utilized BSS algorithm⁴⁴ is a combination of gCKC^{45,46} and fastICA⁴⁷ algorithms. In this method, the number of extracted sources is dependent on the number of iterations in which a new MU is found and also the silhouette threshold that admits sources with high quality. Finally, a fused version is also designed to simultaneously extract a set of temporal and spatial features through its two independent ViT-based parallel paths. The *Macro Path* is the CT-HGR-V1, while the *Micro path* is CT-HGR-V3 fed with the peak-to-peak values of the extracted MUAPs of each source. A fusion path, structured in series to the parallel ones and consisting of FC layers, then combines

Table 8. Comparison of classification accuracy and STD for each fold and their average for each of the 3 models. The accuracy and STD for each fold is averaged over 19 participants.

Model Name	Fold1(%)	Fold2	Fold3	Fold4	Fold5	Average
CT-HGR-V1	79.92 (± 3.39)	91.43 (± 2.48)	93.84 (± 2.05)	92.57 (± 2.28)	88.96 (± 2.83)	89.34 (± 2.61)
CT-HGR-V3	81.53 (± 3.45)	88.03 (± 2.66)	89.63 (± 2.39)	89.11 (± 4.02)	84.92 (± 2.97)	86.64 (± 3.10)
Fused	89.38 (± 2.88)	96.86 (± 1.82)	96.82 (± 1.75)	96.65 (± 2.75)	94.61 (± 1.90)	94.86 (± 2.22)

extracted temporal and spatial features for final classification.

In our experiment, the number of iterations is set to 7 and the silhouette measure is set to 0.92, so a maximum of 7 sources are estimated for each windowed signal. Considering multi-channel sEMG signals as a convolutive mixture of a set of impulse functions known as the MUSTs of each MU⁴⁴, MUSTs are estimated for each electrode channel separately. Therefore, each windowed signal of shape $W \times N_{ch} \times N_{cv}$ is of maximum 7 MUs that retain various activation levels for each electrode channel. As stated in^{48,49}, the activation level/area of MUs in limb muscles is highly variable across different hand gestures. Accordingly, if the peak-to-peak values of MUAPs for each MU and all the channels is calculated, a set of 2D images are acquired which have a predictable pattern among different hand gestures. These 2D images are considered as new input data to the CT-HGR-V3. After training CT-HGR-V1 and V3 individually, the models' weights are kept constant, the final class tokens of each model are joined together and fed to an FC layer for final classification. In such a way, the hybrid model decides based on preprocessed HD-sEMG signals as well as peak-to-peak images of MUAPs obtained for each MU independently. The CT-HGR-V3's hyperparameters are set as follows: For both CT-HGR-V1 and V3, HD-sEMG data is divided into windows of shape (512,8,16) with skip step of 256. So, the image size and the number of input channels for 2D images are set to (8 × 16), 1 respectively. For each peak-to-peak image, we considered 2 patches by setting patch size as (8 × 8). The model's embedding dimension (d) and number of heads is the same as the two previous models. The optimization algorithm is Adam with learning rate of 0.0003 and weight decay of 0.001. Each batch has 64 data samples and the model is trained through 50 epochs. Table 8 compares accuracy and STD for CT-HGR-V1, CT-HGR-V3 and their fused model for each fold.

4 Discussion

Based on the results shown in Table 1 and Table 2, the accuracy for each fold and the average accuracy increases by increasing both the window size and the number of channels. Doubling the number of electrode channels from 32 to 64 results in 2 – 3%, and from 64 to 128 in 1 – 2% increase in all the reported accuracies. Generally speaking, increasing the window size feeds more data points to the model and helps the model to learn more effectively. Along the same line, choosing the same skip step (32 data points) for different window sizes expands the number of input samples to the model and leads to better generalization and higher accuracy. Generalization refers to the ability of the model to make correct predictions for previously unseen data samples. Feeding more data to the model results in more similarity between training and testing samples, hence forcing the network to generate more accurate predictions when new data is delivered. The small skip step (32) chosen here means that the predictions are made every 15.3ms, causing a very small latency for real-time implementation of the proposed network in prosthetic devices. As it is evident from Table 1, starting from 86.23%, the average accuracy increases by 0.3 – 0.8% each time the window size is increased reaching 91.98% when the window size and the number of channels are at the maximum. Therefore, the number of utilized channels, in general, has a greater impact on the accuracy in comparison to the window size. Moreover, the smallest accuracy is for *Fold1* while the highest is for *Fold3/Fold4*, which could be due to the fact that in the first repetition, the subject was not completely aware of the procedure and how to exactly perform the required gesture. Intuitively speaking, the subject was being trained to perform the requested task. We hypothesize that, in the 3rd and 4th repetitions, the subject might have completely learned about the gesture and performed it more consistently, however, in the 5th repetition, fatigue might be a factor resulting in lower performance and relatively large drop in the accuracy.

As can be seen from Fig. 3, choosing the first repetition as the test set considerably differs from choosing the third or fourth repetition as the former yields much lower accuracy on average. STD for each fold and their average follows the same pattern as that of the accuracy, however, in an opposite direction, meaning that the best accuracy is usually associated with the least STD.

As can be seen in Table 2, Model CT-HGR-V2 is generally a better model compared to its CT-HGR-V1 variant as the accuracy for each fold and the overall average are higher. While the best improvement in accuracy occurs for *Fold1* with \approx 1.5% increase compared to CT-HGR-V1, not much improvement (less than 1% in most cases) is observed in the other folds and the final average. As indicated in Table 3, CT-HGR-V2's number of learnable parameters is roughly 3 times the number of learnable parameters of CT-HGR-V1, however, there is a marginal progress in its performance in comparison to the former model. This shows that the hyperparameters used in CT-HGR-V1, producing no more than 100,000 learnable parameters for the model, are sufficient for learning the 66 hand movements with high accuracy and there is no need to use more complex

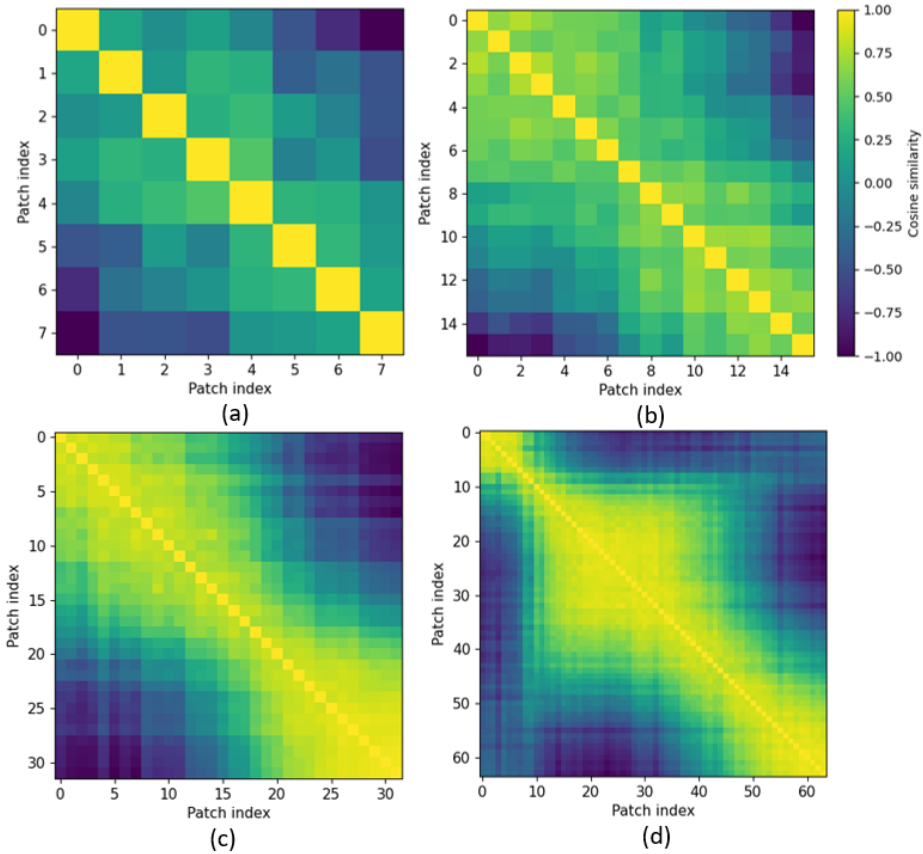


Figure 8. Cosine similarities of repetition 3, subject 20 of CT-HGR-V1 for (a) $W = 64$ (b) $W = 128$ (c) $W = 256$ and (d) $W = 512$

models for hand gesture classification using the proposed CT-HGR framework on this specific HD-sEMG dataset. Clearly, deploying more complex models takes more memory and training time, which in turn reduces the overall efficiency of the model. According to the box plots shown in Fig. 4, all the comparisons between different window sizes are statistically significant. For CT-HGR-V2, we have $p \leq 0.001$ for the $W = 64 / W = 128$ and $W = 256 / W = 512$ pairs, which is less statistically significant than the other pairs with $p \leq 0.0001$. For CT-HGR-V2, the results for the $W = 64 / W = 128$ pair are with $p \leq 0.05$ which is less statistically significant than that for the other pairs.

As mentioned previously, the positional embedding used in the CT-HGR framework is a 1D trainable embedding vector that is added to each of the embedded patches. By increasing the window size in our experiments, the patch size remains constant and the number of patches increases. This causes the positional embedding, which is the principal factor in determination of the input samples' succession, to learn the positions more precisely. Fig. 8 illustrates the cosine similarity matrices of the positional embedding in Model CT-HGR-V1. Cosine similarities are sketched for different window sizes, 128 electrode channels and the trained model on subject 20 when repetition 3 is considered as the test set. In this case, models with window sizes of 64, 128, 256, and 512 have (8, 16) patch sizes. Therefore, each contain 8, 16, 32 and 64 patches in total. The x and y coordinates show the patch indices for each case and each row shows the similarities between each patch and the other patches. The diagonal values in each matrix are the largest values because their positional embedding vector is the same and its cosine is maximum. Similarity in the learned positional embedding vector of patches declines as the patches become farther. For $W = 512$, the model learns the positions better and cosine similarities change more smoothly. Fig. 9 demonstrates the cosine similarity matrices of the positional embedding in Model CT-HGR-V2. Evidently, Model CT-HGR-V2 has learned the position embeddings more effectively as there is less similarity between the distant patches for all the window sizes. The more the window size increases, the more the model discriminates between the distant patches and the more the adjacent patches are considered similar to each other. As illustrated in Fig. 8 and Fig. 9, for $W = 512$, Model CT-HGR-V2 behaves in a more orderly fashion than Model CT-HGR-V1 and consequently, extracts the positional information better.

Regarding instantaneous training, authors in²⁹ implemented a CNN to conduct instantaneous classification of 8 gestures in the CapgMyo DB-a dataset. They applied various pre-processing and hyperparameter tuning steps and achieved a maximum accuracy of 88.1% when all the 128 channels of the electrode grid were utilized. However, we achieved average accuracy

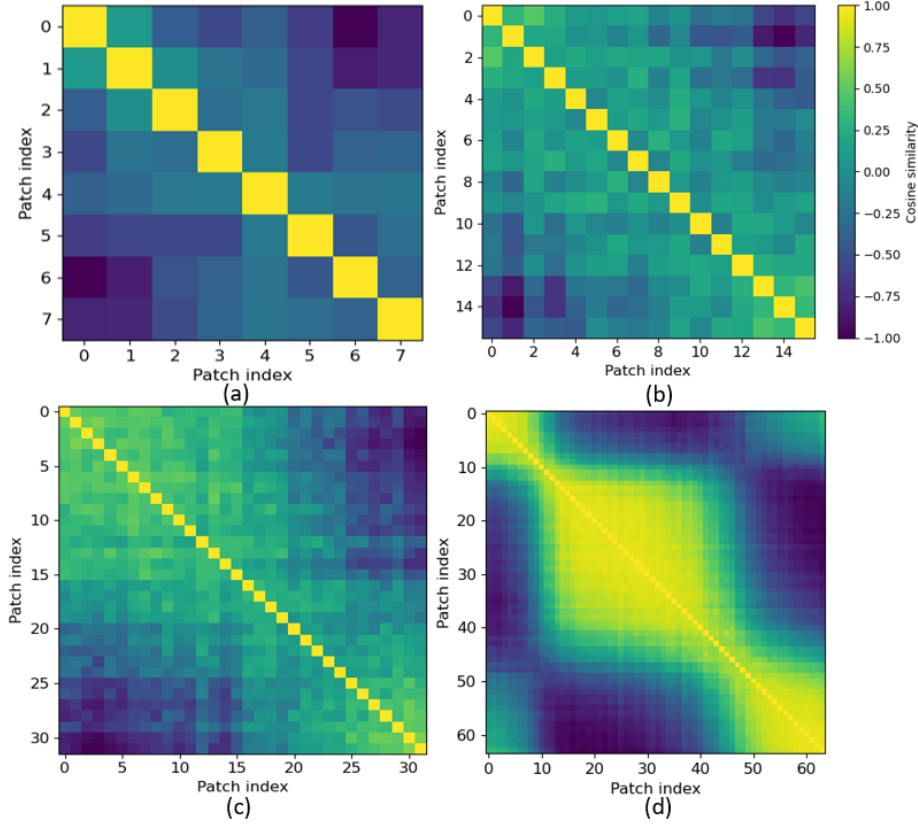


Figure 9. Cosine similarities of repetition 3, subject 20 of CT-HGR-V2 for (a) $W = 64$ (b) $W = 128$ (c) $W = 256$ and (d) $W = 512$

of 89.13% with 64 channels being involved in the study. Based on the results shown in Table 7, no significant discrepancy between the results for instantaneous training and larger window sizes is found. The results, in this case, are very similar to that of CT-HGR-V1, when $W=128$ and number of channels is equal to 64. This suggests that instantaneous training can sometimes work even better than training on very large window sizes with our proposed framework. More specifically, the model is able to achieve high accuracy in learning 66 hand movements with a single-point input which can be considered as an important breakthrough in the field of hand gesture recognition. This proves that HD-sEMG datasets provide highly valuable information of the muscles' activity in each time point which are sufficient for the model to learn various hand gestures with no need for larger window sizes. Furthermore, training with single-point windows of data provides a great number of input samples to the CT-HGR which helps the model generalize better and avoid overfitting. Based on the results shown in Table 6, the average accuracy and STD with shuffling is $\approx 9\%$ higher and $\approx 1.4\%$ lower than the results of the 5-fold cross-validation, respectively. This, however, can cause major issues in practice when dealing with hand prosthetic devices since the test data is entirely unseen and the pre-trained model could not perform reliably while testing with new datasets. In other words, the results reported without shuffling should be used as the bases for practical utilization.

Based on the results shown in Table 4 and Fig. 6, although increasing the window size leads to significant improvements in the average accuracy of the conventional SVM-based model, the achieved accuracy is still lower than the accuracy of the proposed CT-HGR architecture in all the cases. Furthermore, as indicated in Table 5 and Table 3, our proposed CT-HGR framework surpasses the 3D CNN model by $\approx 3\%$ average accuracy while employing less than 1/4 of the learnable parameters used in the 3D CNN model. According to Table 5 and Fig. 6, the accuracy of both the deep networks (CT-HGR-V1 and 3D CNN) increases by less than 1% with doubling the window size. As shown in Fig. 6, there is statistically significant difference among the three models with window size of 64 ($p \leq 0.0001$), implying that the proposed CT-HGR gives its best performance at smaller window sizes. For $W = 128$, the difference between CT-HGR and the other two models is still significant ($p \leq 0.0001$ and $p \leq 0.001$, respectively), but the 3D CNN and SVM do not differ considerably although the 3D CNN is of $\approx 3\%$ more average accuracy than SVM. However, the proposed CT-HGR model seems to perform similarly to SVM when the window size is set to 256 as the p -value in this case is ≥ 0.05 . In this case, there is still significant difference between CT-HGR and 3D CNN architectures with $p \leq 0.0001$.

According to Table 8 in which the studies are reported for the 250 ms window size, CT-HGR-V1's accuracy is higher than

that of the CT-HGR-V3 by $\approx 3 - 4 \%$, except *Fold1* for which the peak-to-peak values of MUAPs provide more accurate information of the performed hand gesture than the HD-sEMG signals. However, a great improvement in average performance of the fused model in comparison to both stand-alone models is witnessed which is 8.22 and 5.52 % increase compared to CT-HGR-V1 and V3, respectively.

5 Conclusion

In this study, we proposed a ViT-based architecture, referred to as the CT-HGR framework, for hand gesture recognition from HD-sEMG signals. Efficacy of the proposed CT-HGR framework is validated through extensive set of experiments with various numbers of electrode channels and window sizes. Moreover, the proposed model is evaluated on instantaneous data samples of the input data, achieving, more or less, a similar accuracy to scenarios with larger window sizes. This provides the context for real-time learning from HD-sEMG signals. Although increasing the number of learnable parameters of the CT-HGR network leads to higher accuracy, the network works reasonably well on 66 hand gestures with less than 65k number of learnable parameters. This is exceptional as its conventional DL-based counterparts have, at times, millions of parameters. Besides, a hybrid model that is trained on raw HD-sEMG signals and their decomposed MUAPs is introduced, which substantially enhances the accuracy of the single CT-HGR model trained solely on raw HD-sEMG data. The sEMG decomposition method utilized in this study, however, is run offline which is considered as a drawback for active prosthetic systems that work in real time. As a direction for the future work, it is interesting to focus on real-time DL-based decomposition of sEMG signals rather than BSS with ICA or gKCK algorithms. In this case, the entire hybrid model can be used in an online fashion for incorporation in advanced HMI systems.

References

1. Li, W., Shi, P. & Yu, H. Gesture recognition using surface electromyography and deep learning for prostheses hand: State-of-the-art, challenges, and future. *Front. neuroscience* 259 (2021).
2. Rahimian, E. *et al.* Fs-hgr: Few-shot learning for hand gesture recognition via electromyography. *IEEE transactions on neural systems rehabilitation engineering* 29, 1004–1015 (2021).
3. Rahimian, E. *et al.* Hand gesture recognition using temporal convolutions and attention mechanism. In *ICASSP 2022-2022 IEEE International Conference on Acoustics, Speech and Signal Processing (ICASSP)*, 1196–1200 (IEEE, 2022).
4. Farina, D., Mohammadi, A., Adali, T., Thakor, N. V. & Plataniotis, K. N. Signal processing for neurorehabilitation and assistive technologies. *IEEE Signal Process. Mag.* 38, 5–7 (2021).
5. Tam, S., Boukadoum, M., Campeau-Lecours, A. & Gosselin, B. Intuitive real-time control strategy for high-density myoelectric hand prosthesis using deep and transfer learning. *Sci. Reports* 11, 1–14 (2021).
6. Chen, W. & Zhang, Z. Hand gesture recognition using semg signals based on support vector machine. In *2019 IEEE 8th Joint International Information Technology and Artificial Intelligence Conference (ITAIC)*, 230–234 (IEEE, 2019).
7. Lee, K. H., Min, J. Y. & Byun, S. Electromyogram-based classification of hand and finger gestures using artificial neural networks. *Sensors* 22, 225 (2021).
8. Leone, F. *et al.* Simultaneous semg classification of hand/wrist gestures and forces. *Front. Neurorobotics* 13, 42 (2019).
9. Zhang, R., Zhang, X., He, D., Wang, R. & Guo, Y. semg signals characterization and identification of hand movements by machine learning considering sex differences. *Appl. Sci.* 12, 2962 (2022).
10. Emayavaramban, G. *et al.* Semg based classification of hand gestures using artificial neural network. *Mater. Today: Proc.* 37, 2591–2598 (2021).
11. Rahimian, E., Zabihi, S., Atashzar, S. F., Asif, A. & Mohammadi, A. Semg-based hand gesture recognition via dilated convolutional neural networks. In *2019 IEEE Global Conference on Signal and Information Processing (GlobalSIP)*, 1–5 (IEEE, 2019).
12. Chen, X., Li, Y., Hu, R., Zhang, X. & Chen, X. Hand gesture recognition based on surface electromyography using convolutional neural network with transfer learning method. *IEEE J. Biomed. Heal. Informatics* 25, 1292–1304 (2020).
13. Azhiri, R. B., Esmaeili, M. & Nourani, M. Real-time emg signal classification via recurrent neural networks. In *2021 IEEE International Conference on Bioinformatics and Biomedicine (BIBM)*, 2628–2635 (IEEE, 2021).
14. Simão, M., Neto, P. & Gibaru, O. Emg-based online classification of gestures with recurrent neural networks. *Pattern Recognit. Lett.* 128, 45–51 (2019).

15. Rahimian, E. *et al.* Temgnet: Deep transformer-based decoding of upperlimb semg for hand gestures recognition. *arXiv preprint arXiv:2109.12379* (2021).
16. Toledo-Peral, C. L. *et al.* semg signal acquisition strategy towards hand fes control. *J. Healthc. Eng.* **2018** (2018).
17. Jiang, N., Dosen, S., Muller, K.-R. & Farina, D. Myoelectric control of artificial limbs—is there a need to change focus?[in the spotlight]. *IEEE Signal Process. Mag.* **29**, 152–150 (2012).
18. Kuruganti, U., Pradhan, A. & Toner, J. High-density electromyography provides improved understanding of muscle function for those with amputation. *Front. Med. Technol.* **41** (2021).
19. Ketykó, I., Kovács, F. & Varga, K. Z. Domain adaptation for semg-based gesture recognition with recurrent neural networks. In *2019 International Joint Conference on Neural Networks (IJCNN)*, 1–7 (IEEE, 2019).
20. Rojas-Martínez, M., Mañanas, M. A. & Alonso, J. F. High-density surface emg maps from upper-arm and forearm muscles. *J. neuroengineering rehabilitation* **9**, 1–17 (2012).
21. Bai, D., Chen, S. & Yang, J. Upper arm motion high-density semg recognition optimization based on spatial and time-frequency domain features. *J. Healthc. Eng.* **2019** (2019).
22. Rojas-Martínez, M. *et al.* High-density surface electromyography signals during isometric contractions of elbow muscles of healthy humans. *Sci. data* **7**, 1–12 (2020).
23. Campanini, I., Disselhorst-Klug, C., Rymer, W. Z. & Merletti, R. Surface emg in clinical assessment and neurorehabilitation: barriers limiting its use. *Front. Neurol.* **934** (2020).
24. Yang, K., Xu, M., Yang, X., Yang, R. & Chen, Y. A novel emg-based hand gesture recognition framework based on multivariate variational mode decomposition. *Sensors* **21**, 7002 (2021).
25. Hu, Y. *et al.* A novel attention-based hybrid cnn-rnn architecture for semg-based gesture recognition. *PloS one* **13**, e0206049 (2018).
26. Xu, P., Li, F. & Wang, H. A novel concatenate feature fusion rcnn architecture for semg-based hand gesture recognition. *PloS one* **17**, e0262810 (2022).
27. Dosovitskiy, A. *et al.* An image is worth 16x16 words: Transformers for image recognition at scale. *arXiv preprint arXiv:2010.11929* (2020).
28. Vaswani, A. *et al.* Attention is all you need. *Adv. neural information processing systems* **30** (2017).
29. Geng, W. *et al.* Gesture recognition by instantaneous surface emg images. *Sci. reports* **6**, 1–8 (2016).
30. Malešević, N. *et al.* A database of high-density surface electromyogram signals comprising 65 isometric hand gestures. *Sci. Data* **8**, 1–10 (2021).
31. Montazerin, M., Zabihi, S., Rahimian, E., Mohammadi, A. & Naderkhani, F. Vit-hgr: Vision transformer-based hand gesture recognition from high density surface emg signals. *arXiv preprint arXiv:2201.10060* (2022).
32. Atzori, M., Cognolato, M. & Müller, H. Deep learning with convolutional neural networks applied to electromyography data: A resource for the classification of movements for prosthetic hands. *Front. neurorobotics* **10**, 9 (2016).
33. Zhang, Z., Yang, K., Qian, J. & Zhang, L. Real-time surface emg pattern recognition for hand gestures based on an artificial neural network. *Sensors* **19**, 3170 (2019).
34. Rahimian, E., Zabihi, S., Atashzar, S. F., Asif, A. & Mohammadi, A. Xceptiontime: independent time-window xceptiontime architecture for hand gesture classification. In *ICASSP 2020-2020 IEEE International Conference on Acoustics, Speech and Signal Processing (ICASSP)*, 1304–1308 (IEEE, 2020).
35. Barsakcioglu, D. Y. & Farina, D. A real-time surface emg decomposition system for non-invasive human-machine interfaces. In *2018 IEEE Biomedical Circuits and Systems Conference (BioCAS)*, 1–4 (IEEE, 2018).
36. Devlin, J., Chang, M.-W., Lee, K. & Toutanova, K. Bert: Pre-training of deep bidirectional transformers for language understanding. *arXiv preprint arXiv:1810.04805* (2018).
37. Ba, J. L., Kiros, J. R. & Hinton, G. E. Layer normalization. *arXiv preprint arXiv:1607.06450* (2016).
38. Côté-Allard, U. *et al.* Deep learning for electromyographic hand gesture signal classification using transfer learning. *IEEE transactions on neural systems rehabilitation engineering* **27**, 760–771 (2019).
39. Lee, K. H., Min, J. Y. & Byun, S. Electromyogram-based classification of hand and finger gestures using artificial neural networks. *Sensors* **22**, 225 (2021).

40. Chen, H., Tong, R., Chen, M., Fang, Y. & Liu, H. A hybrid cnn-svm classifier for hand gesture recognition with surface emg signals. In *2018 International Conference on Machine Learning and Cybernetics (ICMLC)*, vol. 2, 619–624 (IEEE, 2018).
41. Molchanov, P., Gupta, S., Kim, K. & Kautz, J. Hand gesture recognition with 3d convolutional neural networks. In *Proceedings of the IEEE conference on computer vision and pattern recognition workshops*, 1–7 (2015).
42. Chen, J., Bi, S., Zhang, G. & Cao, G. High-density surface emg-based gesture recognition using a 3d convolutional neural network. *Sensors* **20**, 1201 (2020).
43. Alnuaim, A. *et al.* Human-computer interaction with hand gesture recognition using resnet and mobilenet. *Comput. Intell. Neurosci.* **2022** (2022).
44. Negro, F., Muceli, S., Castronovo, A. M., Holobar, A. & Farina, D. Multi-channel intramuscular and surface emg decomposition by convolutive blind source separation. *J. neural engineering* **13**, 026027 (2016).
45. Holobar, A. & Zazula, D. Gradient convolution kernel compensation applied to surface electromyograms. In *International Conference on Independent Component Analysis and Signal Separation*, 617–624 (Springer, 2007).
46. Holobar, A. & Zazula, D. Multichannel blind source separation using convolution kernel compensation. *IEEE Transactions on Signal Process.* **55**, 4487–4496 (2007).
47. Chen, M. & Zhou, P. A novel framework based on fastica for high density surface emg decomposition. *IEEE Transactions on Neural Syst. Rehabil. Eng.* **24**, 117–127 (2015).
48. Zhao, Y. *et al.* Decoding finger movement patterns from microscopic neural drive information based on deep learning. *Med. Eng. & Phys.* **104**, 103797 (2022).
49. Chen, C. *et al.* Hand gesture recognition based on motor unit spike trains decoded from high-density electromyography. *Biomed. signal processing control* **55**, 101637 (2020).

Acknowledgments

This Project was partially supported by Department of National Defence's Innovation for Defence Excellence & Security (IDEaS), Canada, and Natural Sciences and Engineering Research Council (NSERC) of Canada through the NSERC Discovery Grant RGPIN 2019 06966.

Data Availability

The utilized dataset is publicly available through the link provided in Reference³⁰.

Author Contributions Statement

M.M. and E.R. implemented the deep learning models and performed the evaluations; M.M and E.R. drafted the manuscript jointly with F.N. and A.M.; F.A. and S.Y. contributed to the analysis and interpretation and edited the manuscript; F.N. and A.M. directed and supervised the study. All authors reviewed the manuscript.

Additional Information

Competing Interests: Authors declare no competing interests.